

Synthesis of Cu Single Atoms Supported on Mesoporous Graphitic Carbon Nitride and Their Application in Liquid-Phase Aerobic Oxidation of Cyclohexene

Julia Bükér, Xiubing Huang,* Johannes Bitzer, Wolfgang Kleist, Martin Muhler, and Baoxiang Peng*



Cite This: *ACS Catal.* 2021, 11, 7863–7875



Read Online

ACCESS |



Metrics & More



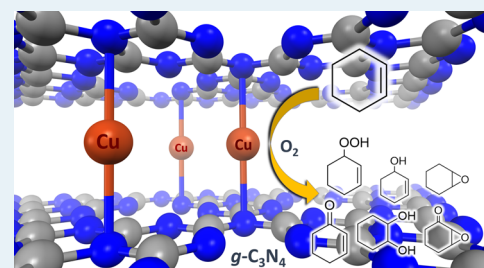
Article Recommendations



Supporting Information

ABSTRACT: Different loadings of Cu single atoms were anchored on a graphitic carbon nitride ($g\text{-C}_3\text{N}_4$) matrix using a two-step thermal synthesis method and applied in liquid-phase cyclohexene oxidation under mild conditions using molecular O_2 as the oxidizing agent. The oxidation state of Cu was determined to be Cu^+ , which is in linear coordination with two neighboring nitrogen atoms at a distance of 1.9 Å. The catalyst with 0.9 wt % Cu pyrolyzed at 380 °C was found to exhibit the best catalytic performance with the highest conversion up to 82% with an allylic selectivity of 55%. It also showed high reusability over four catalytic runs without any detectable Cu leaching. Cyclohexene oxidation followed first-order kinetics with an apparent activation energy of 66.2 kJ mol^{-1} . The addition of hydroquinone as a radical scavenger confirmed that cyclohexene oxidation proceeds via a radical mechanism. Time-resolved *in situ* attenuated total reflection infrared (ATR-IR) spectroscopy was carried out to qualitatively monitor the cyclohexene oxidation pathways. The comparison with the homogeneous analogue Cu(I) iodide indirectly verified the linearly N-coordinated single Cu(I) species to be the active sites for cyclohexene oxidation.

KEYWORDS: cyclohexene oxidation, 2-cyclohexene-1-hydroperoxide, ATR-IR, copper single atoms, EXAFS



1. INTRODUCTION

Selective oxidation of hydrocarbons is of high importance for the chemical industry as it provides access to many high value-added fine chemicals.^{1,2} Over 90% of the globally produced chemicals are manufactured by catalytic processes³ because catalysis is the most economical and energy-saving mode to achieve high conversion and selectivity with low consumption of resources. Nevertheless, many oxidation processes established in the chemical industry are still using toxic oxidizing agents in stoichiometric amounts leading to the coproduction of substantial amounts of environmentally unfriendly and unwanted greenhouse gases such as N_2O as well as inorganic solid waste.² For example, adipic acid has high relevance in the production of synthetic fibers, nylon 6,6, polyurethanes and plasticizers. Its current annual production volume is estimated to be 3.5 million tons,² but it is still produced by oxidizing K/A oil with stoichiometric amounts of HNO_3 , the production of which leads to large quantities of N_2O .^{1,2,4} Therefore, processes using heterogeneous catalysts and more environmentally friendly oxidizing agents are of high interest.

An alternative production route is liquid-phase cyclohexene oxidation, which enables the formation of cyclohexane-1,2-diol as the key product to produce adipic acid by subsequent ring-opening.^{5,6} Cyclohexene oxidation can be carried out using molecular O_2 , which is the most attractive oxidizing agent as it is abundant, inexpensive, and absolutely harmless to the environment.^{1,7} However, selective cyclohexene oxidation is rather

challenging due to the presence of two active bonds in the molecule (Scheme 1).^{7–10} The oxidation at the C–H bond initiates the allylic oxidation leading to the formation of the intermediate 2-cyclohexene-1-hydroperoxide.

This hydroperoxide can be oxidized to 2-cyclohexene-1-one or decomposed to 2-cyclohexene-1-ol, which can also be further oxidized to 2-cyclohexene-1-one. In addition, 2-cyclohexene-1-hydroperoxide can react with 2-cyclohexene-1-one, yielding 7-oxabicyclo[4.1.0]-heptane-2-one.⁹ When oxidation takes place at the C=C double bond, cyclohexene oxide is formed. At the same time, this epoxide is also the product of the reaction of 2-cyclohexene-1-hydroperoxide with another cyclohexene molecule, indicating that the allylic and epoxidation pathways cannot be completely separated from one another. By hydrolysis of cyclohexene oxide, cyclohexane-1,2-diol is formed, which is the key intermediate of liquid-phase cyclohexene oxidation in adipic acid production.¹² Moreover, other reaction products of cyclohexene oxidation are also important building blocks for

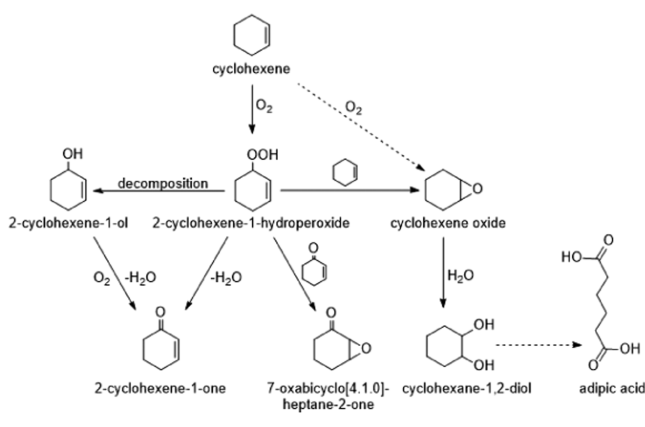
Received: March 31, 2021

Revised: June 7, 2021

Published: June 15, 2021



Scheme 1. Reaction Network of Cyclohexene Oxidation with O₂ as the Oxidizing Agent^{7,9–11}



the synthesis of bulk and fine chemicals, comprising agrochemicals, pharmaceuticals, fragrances, and polymers.^{10,12}

To obtain an increased selectivity despite the wide variety of products of cyclohexene oxidation, it is of great importance to find a suitable catalyst. Recently, single-atom catalysts have attracted extensive attention as they provide maximum efficiency of atom utilization.¹³ The prerequisite is to obtain highly reactive and stable single atoms on an appropriate support, which suppresses their agglomeration under reaction conditions. Graphitic carbon nitride (g-C₃N₄) was found to be a suitable support for single atoms because it enables the efficient anchoring of isolated metal atoms at the nitrogen coordination centers, for example, into the sixfold cavities of the g-C₃N₄ matrix (Scheme S1).^{13–15} Tri-s-triazine was observed to be the elementary building block of g-C₃N₄, and ideal g-C₃N₄ exclusively consists of carbon and nitrogen atoms with a C/N ratio of 0.75.¹⁶ However, until now, no ideally condensed structure has been synthesized, and the as-grown polymers are rich in structural and surface defects rendering g-C₃N₄ a promising support for heterogeneous catalysis.¹⁷ Due to the sp²-hybridized C–N bonds, g-C₃N₄ has a superior tolerance toward high temperatures, and the single-layer stackings based on van der Waals interactions make g-C₃N₄ insoluble in common solvents such as water, alcohols, dimethylformamide, and acetonitrile.^{16,18–21}

Metal-doped g-C₃N₄ has already been successfully applied in several photocatalytic reactions such as H₂ evolution and CO₂ reduction.^{22–30} For example, Zhang et al. reported a bimetallic Ni–Cu cocatalyst supported on g-C₃N₄ synthesized by a template-free preassembly strategy.³¹ Lu et al. studied photocatalytic water splitting over Cu-doped g-C₃N₄ and observed a remarkable increase in anodic photocurrents.³² Gong et al. found Cu-doped mesoporous g-C₃N₄ synthesized by one-step polymerization of melamine to be 2 times more active for photocatalytic methyl orange degradation than the undoped g-C₃N₄.³³ In addition, the application in electrocatalysis has been studied in detail.³⁴ For instance, Dai et al. investigated the electrochemical NO reduction over Cu-decorated g-C₃N₄ and observed that the catalyst efficiently suppressed the competing hydrogen evolution reaction.¹⁴ A similar catalyst synthesized by one-step pyrolysis by Sarkar et al. was found to be highly efficient in the oxygen evolution reaction.³⁵ Recent work has also shown that doped g-C₃N₄ catalysts are suitable for alkane, olefin, or alcohol oxidation reactions.^{36–38} Zhao et al. fabricated Cu single sites on g-C₃N₄ by a preassembly strategy, which achieved a high

degree of conversion of 86% and excellent selectivity of 97% to phenol in benzene oxidation.³¹ However, most of the metal species doped in g-C₃N₄ in the reported literature are embedded in the bulk structure of C₃N₄, which cannot be easily accessed by reactants. To improve the metal atom efficiency and stability, the single-metal atoms should be attached on the surface with suitable interaction with the support.

In the present work, we report for the first time on a series of catalysts consisting of Cu single atoms anchored on g-C₃N₄ using copper disodium ethylenediaminetetraacetic acid (Cu-EDTA) as a precursor by a two-step thermal synthesis method, which was further applied in liquid-phase cyclohexene oxidation with molecular O₂ under mild conditions. The catalysts were characterized in detail by X-ray diffraction (XRD), N₂ physisorption, inductively coupled plasma (ICP), transmission electron microscopy (TEM), energy-dispersive spectrometry (EDS), X-ray photoelectron spectroscopy (XPS), and X-ray absorption spectroscopy (XAS) measurements. The influence of the Cu precursor, the Cu amount, and the pyrolysis temperature on the catalytic properties was studied. Kinetic investigations and a reusability test were performed for the best catalyst. The effects of H₂O and the addition of a radical scavenger were also investigated. *In situ* attenuated total reflection infrared (ATR-IR) spectroscopy was used to monitor cyclohexene oxidation and the complex reaction network. The catalytic activity of a homogeneous analogue catalyst (i.e., CuI) was compared to identify the active sites.

2. RESULTS AND DISCUSSION

2.1. Catalyst Characterization. Cu single atoms were anchored on g-C₃N₄ via a two-step synthesis method. First, g-C₃N₄ was synthesized using Pluronic P123 as a soft-template to achieve high specific surface areas.^{31,39} In the second step, suitable amounts of ethylenediaminetetraacetic acid copper(II) disodium salt (Cu-EDTA) were used to anchor Cu single atoms on the porous g-C₃N₄ targeting at 0.5, 1.0, 1.5, and 2.0 wt % Cu loading. To study the effect of the pyrolysis temperature after the incorporation of Cu into the g-C₃N₄ matrix, the samples were thermally treated at 380 or 500 °C, leading to two temperature series each including four different Cu loadings (Table 1). The samples are labeled “xCu-y”, where *x* is the nominal Cu amount in wt % and *y* is the pyrolysis temperature in °C. ICP-MS measurements were performed to determine the actual Cu loading in the samples. For all samples, ICP-MS analysis shows a lower actual Cu loading compared with the nominal amount of the Cu precursor (Table 1).

Figure 1 shows the XRD patterns of the g-C₃N₄ support and its Cu-containing derivatives. For all samples, distinct reflections at 27.5° were observed, which belong to the (002) lattice plane of g-C₃N₄.^{21,25,40} Additionally, the in-plane structural packing motif (100) at 12.8° can be weakly observed for all samples.⁴⁰ The absence of reflections at high angles indicates the lack of parallel stacking of large numbers of layers.²² The observed slight broadening of the (002) reflections with similar intensities for the Cu-containing samples suggests that the incorporation of Cu atoms does not lead to structural changes in g-C₃N₄. Moreover, no further reflections corresponding to crystalline Cu species were detected, indicating the absence of large Cu nanoparticles. Thus, Cu is most likely to be chemically coordinated to the N atoms in the g-C₃N₄.⁴⁰

The nitrogen adsorption–desorption isotherms of the g-C₃N₄ support and the representative Cu-containing sample 1.5Cu-380 are shown in Figure S1. Both samples exhibit type IV isotherms

Table 1. Cu Loadings Determined by ICP-MS Measurements and Derived Specific Surface Areas, Total Pore Volumes, and Pore Diameters for the g-C₃N₄ Support and Its Cu-Containing Derivatives Based on N₂ Physorption Measurements

sample name	target Cu amount [wt %]	actual Cu amount [wt %]	specific surface area [m ² g ⁻¹]	total pore volume [cm ³ g ⁻¹]	pore diameter [nm]
g-C ₃ N ₄	0.0	0.00	63.3	0.367	34.5
0.5Cu-380	0.5	0.34	61.6	0.338	25.9
1.0Cu-380	1.0	0.84	61.0	0.340	46.6
1.5Cu-380	1.5	0.93	54.1	0.484	43.9
2.0Cu-380	2.0	1.61	58.9	0.395	58.6
0.5Cu-500	0.5	0.36	59.0	0.424	40.1
1.0Cu-500	1.0	0.64	57.3	0.454	28.7
1.5Cu-500	1.5	0.93	52.5	0.375	24.1
2.0Cu-500	2.0	1.79	55.8	0.451	31.8

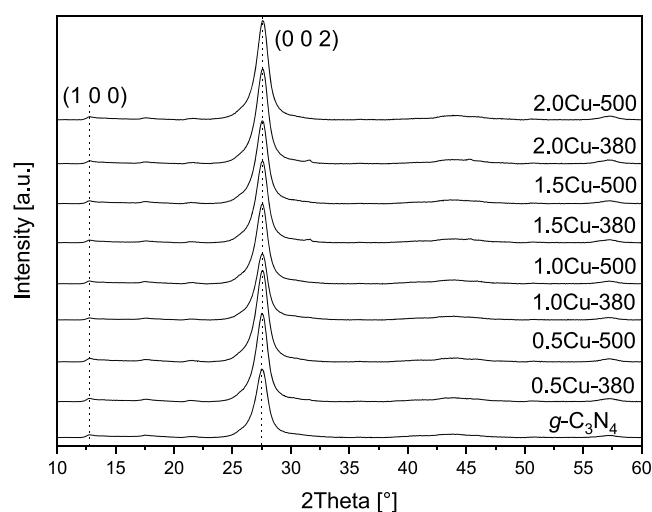


Figure 1. XRD patterns of the g-C₃N₄ support and its Cu-containing derivatives.

with H3 hysteresis loops, indicating a mesoporous material with slit-shaped pores.^{33,41} The specific surface area derived from the Brunauer–Emmett–Teller (BET) method is 63.3 m² g⁻¹ for g-C₃N₄ (Table 1). With increasing Cu amount, a slight decrease in the specific surface area was observed, leading to the lowest surface area of 52.2 m² g⁻¹ for 2.0Cu-380. No strong influence of the different pyrolysis temperatures in the second synthesis step on the specific surface area as well as the total pore volume and the pore diameter derived from the Barrett–Joyner–Halenda (BJH) method was observed. The total pore volumes varied between 0.338 and 0.484 cm³ g⁻¹ accompanied by pore diameters ranging from 24.1 to 58.6 nm (Table 1). Figure S1 shows the corresponding BJH pore size distribution curves, indicating a broad distribution of the pore size for all catalysts. This observation can be explained by the fact that C₃N₄ itself is not a highly porous material and the pores are formed between the C₃N₄ layers.⁴²

The morphology of the samples was investigated by transmission electron microscopy (TEM). Figure 2A,B shows high-angle annular dark field scanning transmission electron microscopy (HAADF-STEM) images of the 1.5Cu-380 sample. An irregular platelet-like structure is observed, and no Cu nanoparticles or clusters are found for all investigated samples (Figure S2), implying that Cu is mainly coordinated to the support as single atoms in agreement with the XRD results (Figure 1). Energy dispersive X-ray (EDX) mapping confirms the uniform distribution of Cu, C, and N (Figure 2D–F), which additionally supports the presumption that Cu is embedded in the g-C₃N₄ matrix.

XP spectra of the g-C₃N₄ support and the samples 0.5Cu-380, 1.5Cu-380, 2.0Cu-380, and 1.5Cu-500 are shown in Figure S3, revealing the presence of small amounts of Cu for the metal-containing samples. Figure 3 shows spectra of 1.5Cu-380 in the C 1s, N 1s, and Cu 2p regions. In the C 1s region, the main peak at 288.1 eV was identified as sp² carbon atoms bound to N in an aromatic ring (C=N–C), while the weak peak at 286.4 eV was assigned to sp³-bound carbon (C–N).^{32,33,43} In the N 1s region (Figure 3B), the main peak at 398.8 eV originates from sp²-hybridized N (C=N–C) and the peak located at 399.6 eV was identified as tertiary N bound to C and the peak at 401.3 eV was caused by π-excitations.²⁴ The Cu 2p spectrum (Figure 3C) shows two symmetrical peaks located at 932.8 and 952.7 eV attributed to Cu 2p_{3/2} and Cu 2p_{1/2}, respectively.^{24,33} No satellite peak was recorded for all samples, indicating the absence of Cu²⁺ species. The differentiation of metallic Cu and Cu(I) species is rather challenging due to the overlapping binding energies and similar splitting of 20 eV. Therefore, the use of the modified Auger parameter allows a more accurate assignment at least for the 2.0Cu-380 sample, where a Cu LMM Auger peak was recorded at a kinetic energy of 914.3 eV. The modified Auger parameter is derived to amount to 1847.1 based on a Cu 2p_{3/2} binding energy of 932.8 eV corresponding to Cu–N–C,⁴⁴ which indicates that Cu is present as Cu⁺ species incorporated into the g-C₃N₄ structure. This can be ascribed to the reduction of Cu–EDTA to Cu⁺ species during pyrolysis.

The surface concentrations of C, N, Cu, and O in the g-C₃N₄ support and the samples 0.5Cu-380, 1.5Cu-380, 2.0Cu-380, and 1.5Cu-500 were determined as well (Table S1). For the g-C₃N₄ support, the C/N ratio is calculated to amount to 0.76, which corresponds to the ratio of 0.75 of defect-free carbon nitrides. A minor increase in the C/N ratio up to 0.87 for 2.0Cu-380 was observed by the incorporation of Cu, confirming the coordination of Cu ions by N atoms.

The different types of C 1s peaks are summarized in Table S2. In the g-C₃N₄ support, 96 atom % of the C atoms are sp²-hybridized. With increasing Cu amount, the concentration decreases to 85.5 atom % in 2.0Cu-380, whereas the N–C and C–C species increase from 2.2 to 8.9 atom % and 1.8 to 5.6 atom %, respectively. These results suggest that the anchoring of Cu atoms in the support matrix leads to structural changes of the aromatic system toward sp³-hybridized N–C and C–C species, but the graphitic carbon nitride structure is still the dominant phase. Moreover, the pyrolysis temperature has a negligible influence on the existing C bonds, as all concentrations of 1.5Cu-500 are similar to those of 1.5Cu-380. For the N atoms, approximately 60% are part of the aromatic system, too, whereas roughly 20% are present as C₃–N species, which are assumed to be the free coordination sites for the Cu species (Table S3).⁴⁵

X-ray absorption spectroscopy (XAS) is a commonly used method to obtain detailed information about the oxidation state

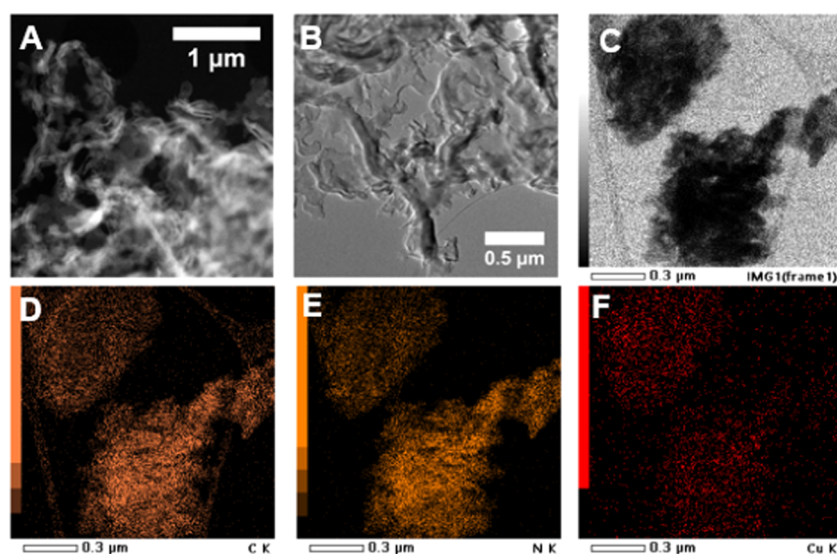


Figure 2. HAADF-STEM images (A–C) and EDX mapping (D–F) of as-synthesized 1.5Cu-380.

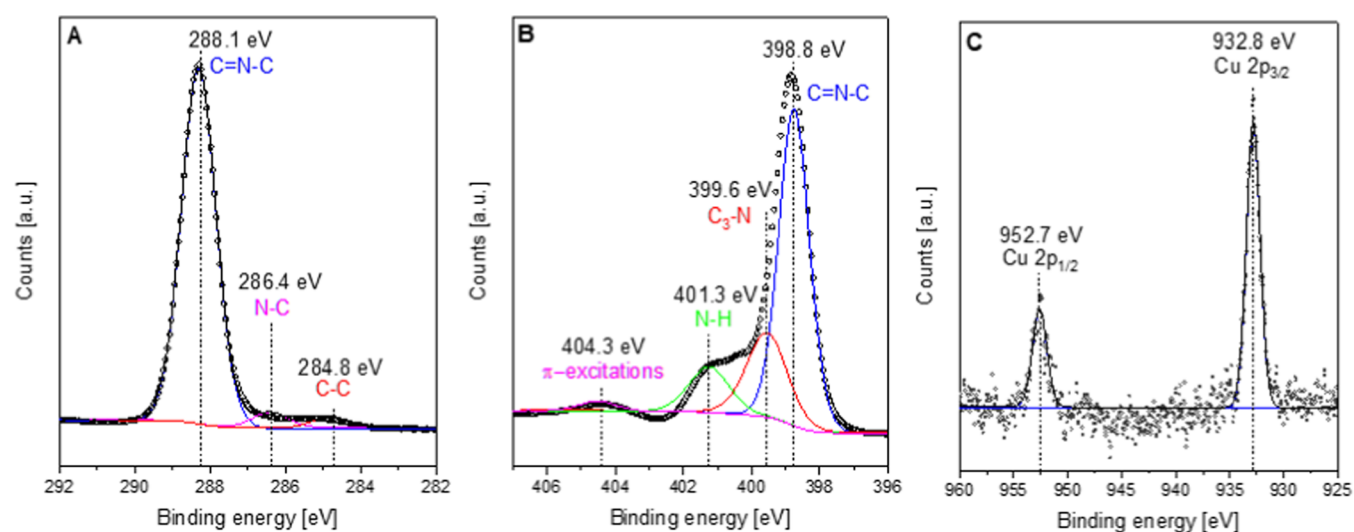


Figure 3. XP spectra of the C 1s (A), N 1s (B), and Cu 2p (C) regions of as-synthesized 1.5Cu-380.

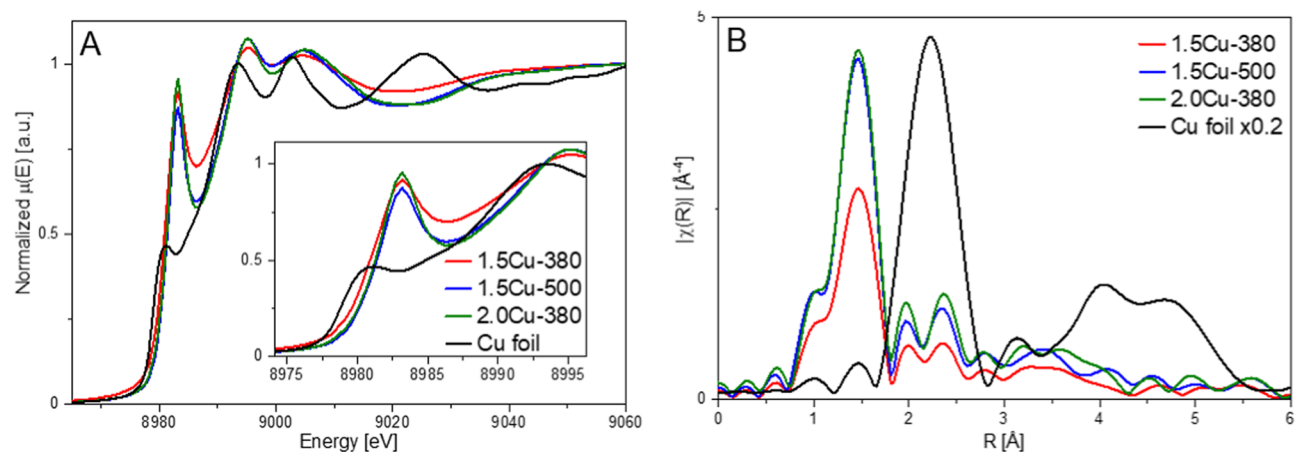


Figure 4. XANES (A) and Fourier-transformed EXAFS spectra (B) of as-synthesized 1.5Cu-380, 1.5Cu-500, and 2.0Cu-380 in comparison to the Cu foil. Note that the Cu foil is multiplied by a factor of 0.2 for better visualization in B. Furthermore, no phase shift corrections have been applied, and the real distances are expected to be ≈ 0.4 Å larger.

and the local chemical environment of metal centers. We recorded XAS spectra for 1.5Cu-380, 1.5Cu-500, and 2.0Cu-380. Based on the X-ray absorption near edge structure (XANES) spectra (Figure 4), the oxidation states of the copper centers in all three materials were determined to be Cu^+ .^{46,47} The edge energy E_0 was shifted to slightly higher energies compared to the reference Cu foil (8979 Cu^0 vs 8981.8 eV samples). For Cu^{2+} , larger shifts to ~ 8985 eV and a pre-edge peak close to 8978 eV ($1s \rightarrow 3d$ dipole forbidden transition) would have been expected.⁴⁷ Due to the $d10$ configuration of Cu^+ , no $1s \rightarrow 3d$ transition, and thus no pre-edge peak was observed. The presence of Cu^+ is also indicated by the strong intensity of the peak at 8983 eV, which is characteristic of Cu^+ in a linear coordination mode and results from a $1s \rightarrow 4p$ transition.^{46,48} The clearly present +1 oxidation state of the Cu centers is particularly remarkable since other publications of Cu on C_3N_4 featured an average oxidation state between +1 and +2.^{31,49} The XANES and the Fourier-transformed extended X-ray absorption fine structure (EXAFS) spectra (Figure 4B) of all three samples differed only slightly. In particular for 1.5Cu-380, the amplitude of the oscillations in the XANES spectra seemed to be dampened compared with the other two materials. However, the recorded spectra in transmission mode did not show this difference, suggesting that this dampening resulted from self-absorption effects. The lower intensity of 1.5Cu-380 in the Fourier-transformed EXAFS spectra might also result from self-absorption effects. Therefore, the Cu loading and the pyrolysis temperature did not seem to have a significant influence on the oxidation state.

The first shell of the Fourier-transformed EXAFS spectra was found at 1.5 Å (note that no phase shift corrections have been applied and the real distances are expected to be ≈ 0.4 Å larger), which is expected for light backscatters like C, N, or O that are coordinated to Cu.

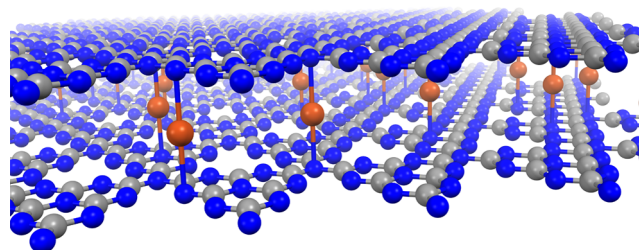
The shells at distances >2 Å displayed only a small intensity, which would be expected for single site Cu centers immobilized on $\text{g-C}_3\text{N}_4$. The comparison of the XANES and the Fourier-transformed EXAFS spectra to literature references confirmed that no Cu^0 , Cu_2O , or CuO was present.

We performed structure fitting based on the Fourier-transformed EXAFS spectra to determine the number of backscatters in the first coordination sphere around the Cu centers (Figure S4 and Table S4). Since it is likely that Cu coordinates to nitrogen, we assumed N as the nearest neighbors, but we cannot unambiguously distinguish C, N, or O due to their similar backscattering properties. In accordance with the linear coordination that was identified from the XANES spectra, approximately two N neighbors were determined by the structure fitting (Table S4). Any additional shell of Cu backscatters from Cu^0 , Cu_2O , or CuO did not result in meaningful fitting results.

Based on these results, we propose the Cu^+ species being coordinated to the C_3N_4 support via two N neighbors in a linear coordination mode as demonstrated in Scheme 2.

2.2. Influence of the Cu Amount, Thermal Treatment Temperature, and Cu Precursor. Cyclohexene oxidation over the as-synthesized Cu- $\text{g-C}_3\text{N}_4$ catalysts was investigated using molecular O_2 as the oxidizing agent. A blank experiment showed only 36.0% cyclohexene conversion and a high hydroperoxide selectivity of 60.0% after 6 h (Figure S7A). $\text{g-C}_3\text{N}_4$ led to a similar degree of conversion and even higher hydroperoxide selectivity above 70%, suggesting that the $\text{g-C}_3\text{N}_4$ support is not able to decompose the intermediate hydro-

Scheme 2. Proposed Structure for the Cu Ions Incorporated into the $\text{g-C}_3\text{N}_4$ Matrix Based on XAS Results^a



^aThe Cu ions are linearly coordinated between two N atoms of two $\text{g-C}_3\text{N}_4$ layers (Cu: red, N: blue, C: gray).

peroxide (Figure S7B). By comparison, Cu-containing $\text{g-C}_3\text{N}_4$ catalysts led to a significantly improved catalytic activity. Figures S5 and S6 show cyclohexene conversion and product selectivity as a function of time over the different catalysts thermally treated at 380 and 500 °C, respectively. For all catalysts, a strong increase in cyclohexene conversion over time was recorded, resulting in high degrees of conversion between 64.7 and 82.3% after 6 h. The use of 1,2-dichlorobenzene as an internal standard for GC analysis revealed carbon balances between 91.2 and 93.4% for all reactions independent of the degree of cyclohexene conversion. The missing amounts are assumed to be the loss of the vapor-phase reactants and products during sampling. All catalysts show high activity toward 2-cyclohexene-1-hydroperoxide decomposition as its initially high selectivity decreases over time, leading to the formation of the desired reaction products. As hydroperoxide is the key intermediate of cyclohexene oxidation, its decomposition plays a crucial role in catalytic conversion. Figures 5 and S8 depict cyclohexene conversion and product selectivity over the four catalysts with different amounts of Cu thermally treated at 380 and 500 °C after 1 and 6 h of reaction, respectively. For the catalysts pyrolyzed at 500 °C (Figure 5B), low degrees of conversion were observed, amounting to 12.8 and 17.3% over 0.5Cu-500 and

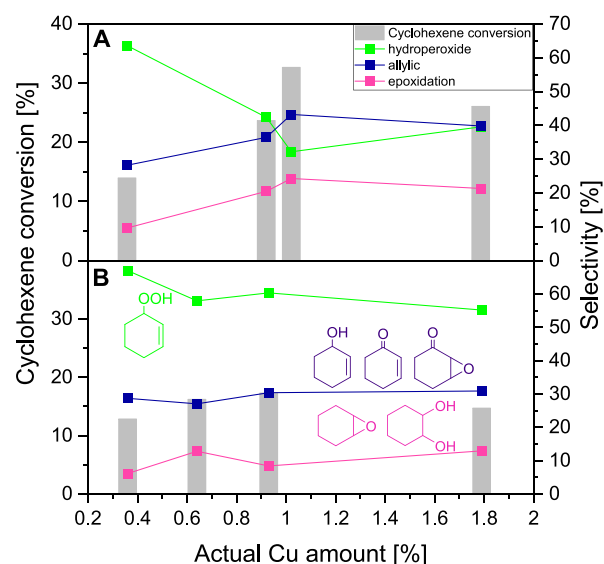


Figure 5. Influence of the Cu amount and pyrolysis temperature on cyclohexene oxidation after 1 h. Cyclohexene oxidation over the samples pyrolyzed at 380 °C (A) and over the samples pyrolyzed at 500 °C (B).

1.5Cu-500, respectively. For all catalysts, similar product selectivities were observed, where 2-cyclohexene-1-hydroperoxide is the main product with a selectivity of roughly 60%. The selectivity to allylic and epoxidation products is nearly constant, independent of the Cu amount incorporated into the catalysts pyrolyzed at 500 °C. After 6 h of reaction, 2-cyclohexene-1-hydroperoxide was still the main reaction product of cyclohexene oxidation with a selectivity of roughly 27%.

Compared with the corresponding sample 0.5Cu-500 pyrolyzed at 500 °C, cyclohexene oxidation over 0.5Cu-380 resulted in a similar conversion and product selectivity (Figure 5A). With increasing Cu amount up to 1.5Cu-380, cyclohexene conversion significantly increased, whereas the selectivity to 2-cyclohexene-1-hydroperoxide decreased by 31.2%, indicating a faster hydroperoxide decomposition. This results in increasing both allylic and epoxidation selectivity by 15.1 and 14.7%, respectively.

Cyclohexene oxidation over the catalysts pyrolyzed at 380 °C is clearly improved compared with the catalysts thermally treated at 500 °C. The best catalyst, 1.5Cu-380, enables a high cyclohexene conversion of 82.3% and a rapid decomposition of 2-cyclohexene-1-hydroperoxide leading to a low selectivity of 12.8% after 6 h. 2-cyclohexene-1-one becomes the main product of cyclohexene oxidation with 24.6% selectivity, followed by cyclohexane-1,2-diol with 17.8%.

The product selectivity is rather similar for all catalysts thermally treated at 380 °C, suggesting that the active Cu centers are mainly involved in the decomposition of 2-cyclohexene-1-hydroperoxide, which is strongly affected by the increasing Cu amount up to a loading of 1.5 wt %. The slight decrease of hydroperoxide decomposition ability over the 2.0Cu-380 catalyst is assumed to result from the enhanced C/N ratio (Table S1) and the lower concentration of C₃-N free coordination sites (Table S3). In conclusion, pyrolysis at the lower temperature of 380 °C enables higher degrees of cyclohexene conversion, faster hydroperoxide decomposition, and higher selectivity to allylic products.

In addition to the pyrolysis temperature, the influence of the Cu precursor was studied using Cu(NO₃)₂·3H₂O instead of Cu-EDTA (Figure S10).²⁴ The characterization of the nitrate-based catalyst 1.5Cu-380-NO₃ also indicated successful Cu anchoring in the g-C₃N₄ matrix and a high Cu distribution (Figure S9). However, cyclohexene oxidation over 1.5Cu-380-NO₃ resulted in a significantly lower degree of cyclohexene conversion of only 58.4% compared with 82.9% over 1.5Cu-380. Moreover, a strong increase in hydroperoxide selectivity was observed for 1.5Cu-380-NO₃ resulting in lower product selectivities, especially for cyclohexane-1,2-diol.

2.3. Kinetic Investigations over 1.5Cu-380. The best catalyst, 1.5Cu-380, was selected to perform kinetic studies on cyclohexene oxidation. The continuous increase in cyclohexene conversion as a function of temperature is presented in Figures 6A and S12A–C. A high degree of conversion of 94.9% was already reached after 4 h at 100 °C. With increasing temperature, a strikingly lower hydroperoxide selectivity was observed, which decreased from 50.0% after 6 h at 60 °C to 0.0% at 100 °C, confirming a complete decomposition of the reaction intermediate at the elevated temperature. The fast hydroperoxide decomposition resulted in higher product selectivities, which increased by 8.7, 7.7, 9.6, and 6.0% for 2-cyclohexene-1-one, cyclohexene oxide, 7-oxabicyclo-[4.1.0]heptane-2-one, and cyclohexane-1,2-diol, respectively. Only 2-cyclohexene-1-ol selectivity was not affected, indicating its further oxidation to

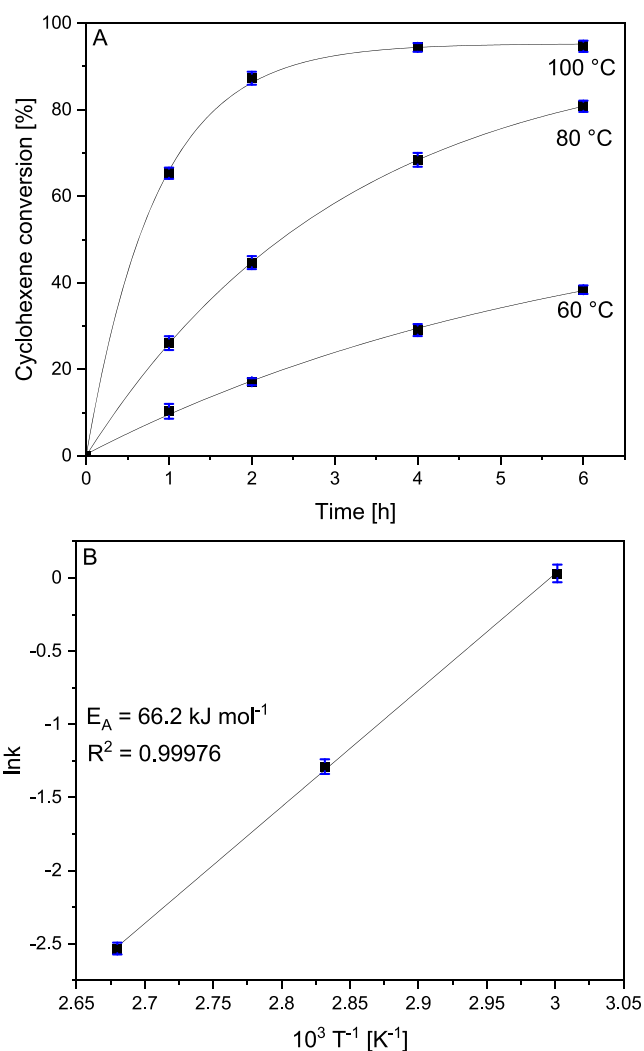


Figure 6. Kinetic investigations of cyclohexene oxidation over 1.5Cu-380. The degree of cyclohexene conversion as a function of time at different temperatures (A) and the Arrhenius plot based on first-order kinetics (B).

2-cyclohexene-1-one (Scheme 1). The increase in selectivity and cyclohexene conversion with increasing temperature from 60 to 100 °C led to an increased total product yield of oxidation products by 35.4–68.8% after 6 h. For all temperatures, an increase of the ketone/alcohol ratio over time was observed (Figure S12D). Furthermore, the ketone/alcohol ratio was increased with increasing temperature suggesting a selectivity shift to 2-cyclohexene-1-one at elevated temperatures. This observation indicates the promotion of the further oxidation of 2-cyclohexene-1-ol to 2-cyclohexene-1-one or 2-cyclohexene-1-hydroperoxide into 2-cyclohexene-1-one (Scheme 1). The ratio of allylic reaction products including 2-cyclohexene-1-one, 2-cyclohexene-1-ol, and 7-oxabicyclo[4.1.0]heptane-2-one to the epoxidation products cyclohexene oxide and cyclohexane-1,2-diol also shows a significant temperature dependence (Figure S12D). This ratio strongly decreases with increasing temperature, indicating the preferential formation of epoxidation products at higher temperatures. Therefore, higher reaction temperatures were found to promote the formation of epoxidation products and to shift the allylic selectivity toward 2-cyclohexene-1-one.

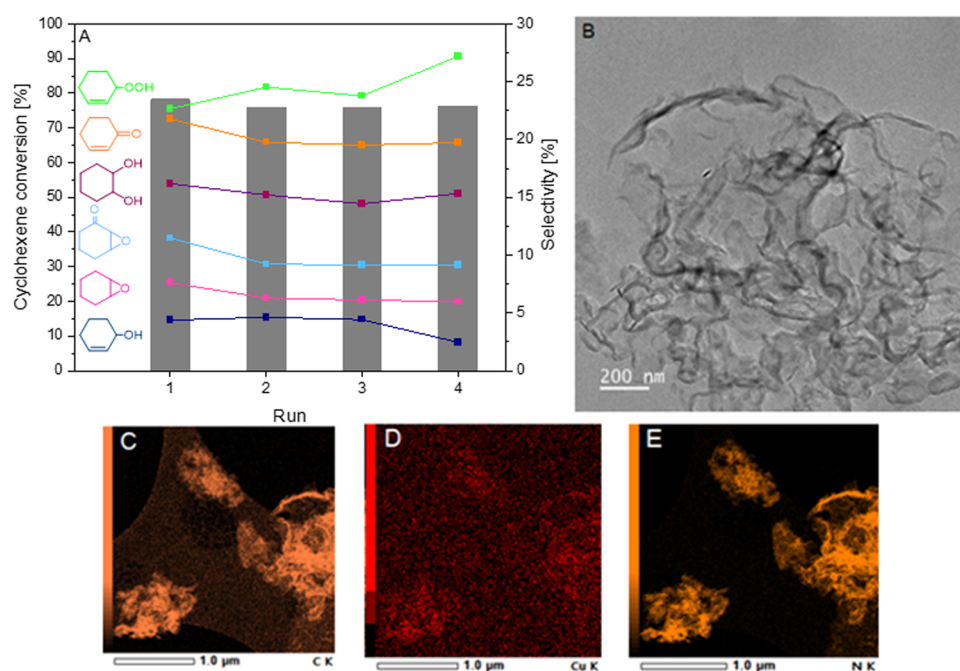


Figure 7. Reusability test for cyclohexene oxidation over 1.5Cu-380. The degree of conversion and selectivity as a function of time (A), STEM image (B), and EDX mappings (C–E) of the spent 1.5Cu-380 catalyst after four cycles.

The time curves of cyclohexene oxidation at 60, 80, and 100 °C were used for Arrhenius analysis (Figure 6A). The linearized plot for first-order reaction kinetics is well suited for linear regression ($R^2 > 0.995$), suggesting that cyclohexene oxidation over 1.5Cu-380 follows first-order reaction kinetics (Figure S12E). The Arrhenius analysis results in an apparent activation energy of 66.2 kJ mol⁻¹ (Figure 6B).

2.4. Reusability Test. The reusability test over 1.5Cu-380 was performed to study the catalyst stability in terms of activity and selectivity toward cyclohexene oxidation as well as the stability of the anchored Cu single atoms in the g-C₃N₄ matrix. After four reaction cycles, the degree of cyclohexene conversion was still stable amounting to 78.2, 75.8, 75.9, and 76.3% for the consecutive runs (Figure 7A). To investigate its stability, an XRD pattern of the spent catalyst was recorded after four reaction runs. An identical pattern compared with the fresh catalyst was obtained, providing no indication of structural changes of the g-C₃N₄ support or formation of large crystalline Cu species (Figure S13A). ICP-MS measurements excluded the presence of Cu in the solution, confirming that there is no Cu leaching due to the strong coordination of the Cu ions to the N atoms in the g-C₃N₄ matrix. The recorded XP spectrum of the spent 1.5Cu-380 catalyst reveals similar surface concentrations of Cu, C, O, and N (Table S5) as well as equal peak positions for the Cu 2p_{1/2} and 2p_{3/2} signals, which would be expected to shift to higher binding energies if Cu²⁺ species were present (Figure S13). In addition, the STEM image does not indicate structural changes of the catalyst or the formation of Cu nanoparticles either (Figure 7B). EDX mapping still reveals a uniform elemental distribution of Cu, C, and N on the catalyst surface (Figure 7C–E) so that XRD, ICP, STEM, EDX, and XPS measurements confirm the high stability of the catalyst observed over four consecutive runs of cyclohexene oxidation.

2.5. Time-Resolved *In Situ* ATR-IR Spectroscopy. As shown in the previous investigations, cyclohexene oxidation follows a complex reaction network, which can lead to the formation of several oxidation products (Scheme 1). The

numerous reaction paths impede selective cyclohexene oxidation to one desired product, hence the search for highly selective catalysts is rather challenging. To clarify the different reaction pathways of cyclohexene oxidation, the reaction was investigated by *in situ* ATR-IR spectroscopy, which enables the time-resolved monitoring of cyclohexene oxidation and product formation. Characteristic vibrations of cyclohexene and several possibly formed reaction products were assigned by recording spectra of the pure compounds (Table S6). Until now, the assignment of the intermediate 2-cyclohexene-1-hydroperoxide has not been possible yet, as its characteristic vibrations are found to be very weak and overlapping with several vibrations of cyclohexene and its oxidation products.⁵⁰ We succeeded in synthesizing a solution of 2-cyclohexene-1-hydroperoxide with a high concentration of 65% (Figure S14A) and recorded the spectra of the mixture dissolved in acetonitrile (Figure S14B). The addition of three times each 1 mL of the 2-cyclohexene-1-hydroperoxide solution resulted in similar spectra with increasing intensities. 2-Cyclohexene-1-one (1685 cm⁻¹) and 2-cyclohexene-1-ol (1064 cm⁻¹) as well as two unknown signals at 1036 and 949 cm⁻¹ were identified. To determine the characteristic signal of the hydroperoxide, triphenylphosphine (PPh₃) was added to selectively decompose 2-cyclohexene-1-hydroperoxide into 2-cyclohexene-1-ol. With increasing PPh₃ amount added to the mixture, the signals at 1036 and 949 cm⁻¹ vanished, whereas the characteristic signal of 2-cyclohexene-1-ol increases suggesting these signals to correspond to 2-cyclohexene-1-hydroperoxide. The intensity of the signal assigned to 2-cyclohexene-1-one was retained, confirming the selective decomposition of 2-cyclohexene-1-hydroperoxide into 2-cyclohexene-1-ol.

Based on this knowledge, *in situ* ATR-IR spectroscopy of cyclohexene oxidation was carried out. The reaction progress was continuously monitored by recording the spectra every 2 min. The reaction was initiated by pressurizing the heated solution with molecular O₂ and the corresponding spectrum was used for background correction. Figure S15 depicts the recorded

spectra of cyclohexene oxidation over 1.5Cu-380 over 6 h. A significant decrease of the C–H bending vibration at 725 cm^{-1} was recorded, demonstrating the consumption of cyclohexene during cyclohexene oxidation. A strong increase in the intensity was observed for the stretching vibration of a carbonyl group at 1694 cm^{-1} , which corresponds to the formation of 2-cyclohexene-1-one. In addition, the signals at 1036 and 952 cm^{-1} assigned to 2-cyclohexene-1-hydroperoxide increased over time. Moreover, higher intensities over time were recorded for the stretching vibrations at 1096 , 1075 , and 1010 cm^{-1} , which indicate the formation of cyclohexene oxide, cyclohexane-1,2-diol, and 2-cyclohexene-1-ol, respectively. Figure 8A shows the

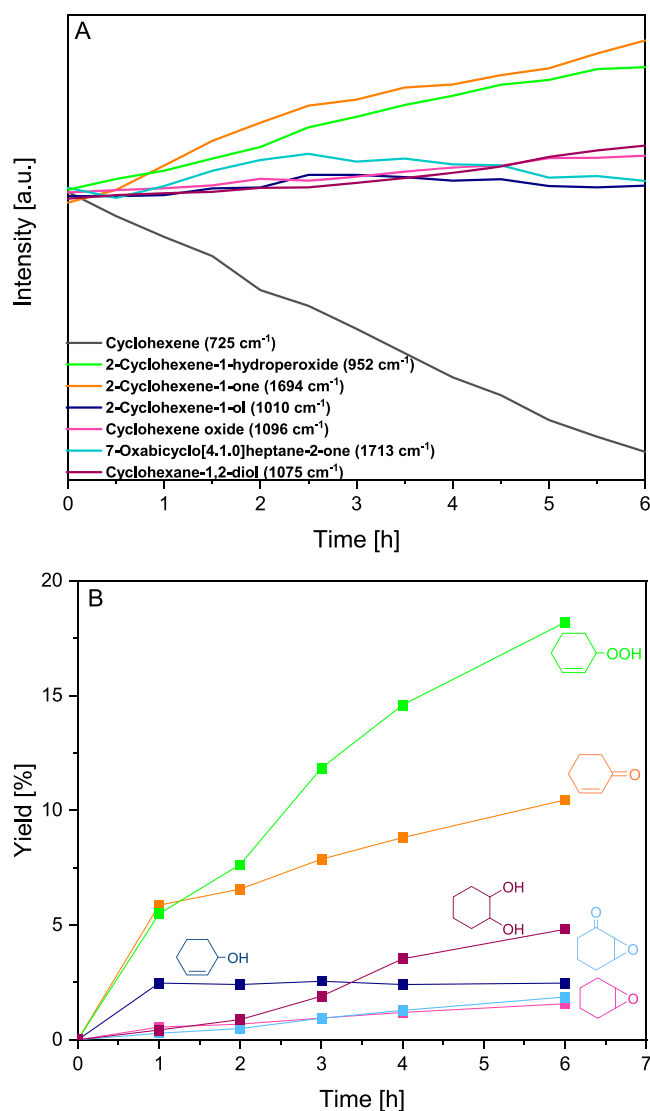


Figure 8. Quantitative trends of the assigned vibrations recorded during *in situ* ATR spectroscopy (A) and product yields of cyclohexene oxidation during *in situ* ATR spectroscopy quantified by GC analysis (B).

time-resolved relative trends of the assigned compounds, which again demonstrate the consumption of cyclohexene and the formation of the corresponding reaction products. In addition to ATR spectroscopy, offline samples were analyzed by GC to determine the formation of reaction products quantitatively (Figure 8B). 2-Cyclohexene-1-hydroperoxide was examined to be the main product of cyclohexene oxidation with a yield of

18.2%. In addition, *in situ* ATR-IR spectroscopy showed that hydroperoxide is the first product that is formed in cyclohexene oxidation, confirming the proposed reaction network (Scheme 1). The formation of all other reaction products started within the first 30 min, and the highest reaction rate was observed for 2-cyclohexene-1-one, which was formed with the second highest yield over the whole investigated time period indicating the successful oxidation of 2-cyclohexene-1-hydroperoxide to 2-cyclohexene-1-one (Scheme 1). In agreement with the quantitative GC analysis, the vibrations at 1010 cm^{-1} assigned to 2-cyclohexene-1-ol stays at the same intensity after 1 h, whereas the band of 2-cyclohexene-1-one arises, consequently suggesting 2-cyclohexene-1-ol to be further oxidized to 2-cyclohexene-1-one. This observation was previously discussed by Maschmeyer et al., who found an equilibrium concentration of cyclohexanol in cyclohexene oxidation.⁵¹ Moreover, the consecutive pathway from cyclohexene oxide to cyclohexane-1,2-diol can be confirmed by these results, as cyclohexene oxide is formed first followed by the formation of cyclohexane-1,2-diol, whereas the cyclohexene oxide yield remained constant (Figure 8).

2.6. Mechanistic Investigations. The influence of H_2O on cyclohexene oxidation is studied since H_2O is formed in several oxidation reaction steps as a byproduct of cyclohexene oxidation and, in addition, H_2O is consumed by the hydrolysis of cyclohexene oxide to form cyclohexane-1,2-diol (Scheme 1). Therefore, 2 mL of H_2O was added to the standard solution. Figure S16A shows cyclohexene oxidation over 1.5Cu-380 in the absence of H_2O , whereas Figure S16B shows cyclohexene conversion and selectivity over time with H_2O addition. The reaction rate of cyclohexene oxidation is drastically lowered by H_2O addition, as cyclohexene conversion decreased from 82.9 to 64.2% after 6 h. The addition of H_2O led to a significantly enhanced 2-cyclohexene-1-hydroperoxide selectivity of 67.2% after 1 h and 34.9% after 6 h, while in the absence of H_2O , initial hydroperoxide selectivity was determined to be 39.5 and 15.2% after 6 h. Consequently, the initial selectivity to cyclohexane-1,2-diol, 7-oxabicyclo[4.1.0]-heptane-2-one, and 2-cyclohexene-1-one was strongly decreased by 12.3, 9.0, and 8.8%, respectively. Meanwhile, 2-cyclohexene-1-ol selectivity remained constant leading to the assumption that the 2-cyclohexene-1-hydroperoxide decomposition step to form 2-cyclohexene-1-ol is not affected by the presence of H_2O , whereas the reaction steps where H_2O is produced as the byproduct are significantly suppressed (Scheme 1). Likewise, the cyclohexene oxide selectivity is similar over the whole period of time and independent of the addition of H_2O . As the overall catalytic activity is decreased when adding H_2O , it can be concluded that H_2O probably blocks the active Cu centers of the catalyst. Although H_2O is needed for the hydrolysis of cyclohexene oxide to cyclohexane-1,2-diol, a lower selectivity to the diol was observed, suggesting that hydrolysis catalyzed by active Cu sites was also blocked by H_2O . Moreover, the presence of H_2O suppresses reactions where H_2O is produced as the byproduct. To verify whether cyclohexene oxidation over 1.5Cu-380 also proceeds via a radical mechanism as found earlier, 20 mol % hydroquinone was added to the solution acting as a radical scavenger. Even after 6 h, no cyclohexene conversion was observed, indicating that cyclohexene oxidation completely proceeds via a radical mechanism.¹⁰ Cyclohexene conversion in the absence of any catalyst was found to result in the same data compared with the reaction in the presence of the $\text{g-C}_3\text{N}_4$

support, confirming Cu as an active site for cyclohexene oxidation (Figure S7).

XPS and EXAFS measurements identified the oxidation state of the Cu species to be 1+. For this reason, Cu(I) iodide as a homogeneous analogue of our heterogeneous Cu catalyst was used for cyclohexene oxidation to determine the activity of Cu(I) species in homogeneous solution (Figure S17). Cu(I) is known to form bidentate complexes in acetonitrile (Scheme S2), and the Cu ion is linearly coordinated to two N atoms,⁵² which is rather similar to our proposed single-atom catalyst (Scheme 2). The initial reaction rates of cyclohexene oxidation and hydroperoxide decomposition over the homogeneous catalyst were significantly enhanced. However, only a slightly higher degree of cyclohexene conversion of 87.8% was observed over Cu(I) iodide compared with 1.5Cu-380 after 6 h. In addition, the product selectivities using the homogeneous and heterogeneous catalysts are nearly equal. These results indicate that Cu(I) species are mainly involved in the decomposition of the reaction intermediate 2-cyclohexene-1-hydroperoxide. More importantly, the comparable catalytic activity of the Cu(I) bidentate complexes in Cu(I) iodide to our Cu single-atom catalyst 1.5Cu-380 verifies the presence of Cu(I) species and the proposed linearly coordinated Cu(I) species with two N atoms indirectly.

Despite the anchoring of the Cu atoms on the g-C₃N₄ support, these catalysts enable a similarly high degree of interaction with the substrate as homogeneous catalysts, as shown by the catalytic data. The high catalytic activity of Cu(I) species can be attributed to its coordinatively unsaturated nature. The high catalytic activity of coordinatively unsaturated sites (CUS) in single-atom catalysts has been investigated by Zhang et al., who studied the selective oxidation of C–H bonds with *tert*-butylhydroperoxide over atomically dispersed FeN_x species.⁵³ They found the unsaturated Fe(III)N₅ site to be the most active with a high tendency for homolytic cleavage of the *tert*-butylhydroperoxide-forming radicals. Investigations on CO oxidation over a defect-engineered HKUST-1 metal–organic framework by Wöll et al. demonstrated the excellent catalytic activity of defect Cu⁺.⁵⁴ Bao et al. studied the catalytic activity of exposed Cu–N active sites within graphene toward oxygen reduction for zinc–air batteries.⁵⁵ Based on density functional theory (DFT) calculations, the Cu(I)–N₂ site was examined to reveal a superior catalytic activity toward ORR in comparison with Cu–N₃ and Cu–N₄ due to its high potential to bind and activate O₂. Moreover, Cu(I) species were found to be highly active for decomposition of hydroperoxides into radicals⁵⁶ according to the Haber–Weiss mechanism, which is an important feature in cyclohexene oxidation (Scheme 1). An example of catalyzed oxidation reactions by single Cu centers in nature is the dopamine- β -monooxygenase (D β M), which catalyzes the C–H bond activation by performing a Cu(I)–D β M complex. This complex then reacts with O₂ by forming a Cu hydroperoxide, which hydroxylates the substrate.^{57,58} All of these examples show that Cu(I) species are highly active toward C–H bond activation and hydroperoxide decomposition, which are the key steps of cyclohexene oxidation. The herein presented single Cu atom catalyst revealed excellent stability toward cyclohexene oxidation with nearly no loss in catalytic activity compared with the homogeneously catalyzed reaction. Thus, we succeeded in heterogenizing single Cu(I) species, which facilitates their separation and reuse. Consequently, this material is a promising catalyst for combining the advantages of homogeneous and heterogeneous catalysis.

3. CONCLUSIONS

Cu single ions with uniform distribution were successfully anchored on mesoporous g-C₃N₄ with different loadings via chemical coordination to C₃–N species using Cu–EDTA as the precursor. It was confirmed by XRD, TEM, and EDX that the Cu ions were uniformly distributed over the support, and their incorporation did not change the structure of the g-C₃N₄ matrix. XPS and XANES measurements determined the oxidation state of the Cu centers to be Cu⁺. The distance between the Cu centers and their direct neighbors was determined to be 1.9 Å, which can be assigned to Cu presumably coordinated to N. The linear coordination of Cu was proposed based on the EXAFS spectra, indicating two neighbors coordinated to the Cu centers.

An improved catalytic activity for the cyclohexene oxidation using molecular oxygen as the oxidizing agent was found for the Cu–g-C₃N₄ catalysts thermally treated at 380 °C. A lower pyrolysis temperature of 380 °C resulted in higher degrees of conversion and enhanced hydroperoxide decomposition leading to higher allylic selectivities. Interestingly, the selectivity to epoxidation products remained constant. Cu–EDTA was found to be a suitable Cu precursor for the synthesis of Cu single atoms anchored on g-C₃N₄, as the alternative use of Cu(NO₃)₂ revealed a significantly lower degree of cyclohexene conversion as well as a significantly decreased cyclohexane-1,2-diol selectivity. Kinetic investigations over the best catalyst, 1.5Cu-380, determined cyclohexene oxidation to follow first-order reaction kinetics with an apparent activation energy of 66.2 kJ mol^{−1}. The catalyst was also found to be highly reusable. The addition of H₂O resulted in a drastic decrease of conversion due to the blocking of the active Cu⁺ centers by H₂O. By adding the radical scavenger hydroquinone, we confirmed that cyclohexene oxidation proceeds via a radical mechanism. Time-resolved *in situ* ATR-IR spectroscopy was employed to monitor the reaction progress and confirmed the complex reaction network spectroscopically. The comparison with the homogeneous catalyst Cu(I) iodide identifies the Cu(I) species linearly coordinated to two N atoms as the active sites with a high catalytic activity due to their coordinatively unsaturated nature. Cyclohexene oxidation over Cu(I) iodide resulted in similar catalytic data identifying the single Cu atom material as a promising heterogeneous catalyst for cyclohexene oxidation, enabling significantly easier catalyst separation and reusability. Our work provides an easy strategy to prepare supported transition metal single atoms on g-C₃N₄ with high catalytic activity and excellent stability.

4. EXPERIMENTAL SECTION

4.1. Materials. For Cu–C₃N₄ synthesis, Pluronic P123, melamine (99%), sulfuric acid (95–98%), Cu–EDTA (>97%), and Cu(NO₃)₂·3H₂O (99%) were purchased from Sigma-Aldrich. Methanol in analytical reagent grade was bought from Fisher Chemicals.

For cyclohexene oxidation, cyclohexene (99%), 2-cyclohexene-1-one (98%), 2-cyclohexene-1-ol (95%), cyclohexene oxide (98%), 7-oxabicyclo[4.1.0]heptane-2-one (98%), cyclohexane-1,2-diol (98%), and 1,2-dichlorobenzene (99%) were purchased from Sigma Aldrich. Acetonitrile in analytical reagent grade was bought from Fisher Chemicals. All reagents were employed without further purification.

4.2. Catalyst Synthesis. For the synthesis of g-C₃N₄, 5 g of Pluronic P123 and 25 g of melamine were dissolved in 100 mL of deionized H₂O. The solution was stirred at 100 °C. After 1 h, 10

mL of sulfuric acid solution ($\text{H}_2\text{SO}_4/\text{H}_2\text{O}=1:1$ volume) was added dropwise, and a white precipitate was obtained. The precipitate was filtered off after the solution was cooled down to room temperature and dried in a hot-air oven at $80\text{ }^\circ\text{C}$ overnight. The obtained powder was heat-treated in Ar at $600\text{ }^\circ\text{C}$ for 4 h in a quartz tube. Afterward, it was calcined at $550\text{ }^\circ\text{C}$ for 2 h.

For the preparation of Cu– C_3N_4 catalysts, 0.5 g of C_3N_4 was dispersed in 40 mL of methanol. A calculated amount of Cu–EDTA was added for obtaining 0.5, 1.0, 1.5, and 2.0 wt % Cu loadings, and the dispersion was stirred for several hours at room temperature until the solvent was evaporated. The obtained powder was dried at $80\text{ }^\circ\text{C}$ overnight and thermally treated under inert He flow for 2 h at 380 and $500\text{ }^\circ\text{C}$. For comparison, a catalyst with 1.5 wt % Cu on g- C_3N_4 was synthesized using $\text{Cu}(\text{NO}_3)_2\cdot 3\text{H}_2\text{O}$ as the precursor and the same procedure as described above.

4.3. X-ray Diffraction (XRD) Measurements. X-ray diffraction measurements were carried out with a Bruker D8 Discover X-ray diffractometer. As the X-ray source, $K\alpha$ radiation with a wavelength of 1.5401 \AA was used. The patterns were recorded in a 2θ range from 20 to 60 with a scan step size of 0.02° using a continuous scan mode with a scan time of 1 s per step and a rotation of 5 rpm. Evaluation of the recorded diffraction pattern was conducted using High Score Plus software equipped with access to the International Centre for Diffraction Data (ICDD) database.

4.4. N_2 Physisorption Experiments. N_2 physisorption measurements were performed at 77 K in a BEL-mini apparatus. The as-prepared powders were first degassed at $120\text{ }^\circ\text{C}$ under vacuum for 6 h to remove adsorbed water. The specific surface areas were determined from the adsorption isotherms using the BET method. The pore volume and the pore size distribution were obtained by applying the BJH method.

4.5. High-Resolution Transmission Electron Microscopy (HR-TEM). High-resolution and high-angle annular dark field scanning transmission electron microscopy (HR-TEM, HAADF-STEM) and energy dispersive X-ray spectroscopy (EDX) characterization was performed using a probe-side aberration-corrected JEM-2200FS (JEOL, Akishima, Japan) with an acceleration voltage of 200 kV. For sample preparation, nanoparticles were dispersed in ethanol for 5 min with ultrasonic treatment, and the dispersions of the nanoparticles were added dropwise on a carbon-coated gold grid for TEM measurements.

4.6. Inductively Coupled Plasma Mass Spectroscopy (ICP-MS). ICP-MS measurements were carried out in a Thermo Fisher iCAP RQ using a KED (kinetic energy discrimination) cell and a quadrupole mass spectrometer. For digestion, 10 mg of the sample was treated with 4 mL of HNO_3 and 0.5 mL of HClO_4 in a microwave system.

4.7. X-ray Photoelectron Spectroscopy (XPS). XPS was performed in an ultrahigh vacuum setup equipped with a Gammatdata Scienta SES 2002 analyzer. The spectra were obtained at a pass energy of 200 eV at a base pressure of 6×10^{-10} mbar with monochromatic Al $K\alpha$ radiation (1486.3 eV, 14.5 kV, 45 mA). The C 1s peak at 284.8 eV was used as the reference. The deconvolution of the spectra was performed using CasaXPS software with Shirley-type background subtraction and symmetric and asymmetric Gaussian–Lorentzian line shapes.

4.8. X-ray Absorption Spectroscopy (XAS). XAS experiments were performed at PETRA III Extension beamline P65 (energy range: 4–44 keV) at DESY (Deutsches Elektronensynchrotron) in Hamburg (Germany).⁵⁹ A Si(311) C-type

double crystal monochromator was used for the measurements at the Cu K-edge. The beam current was 100 mA with a ring energy of 6.08 GeV. The samples were measured in glass capillaries without dilution. All spectra were recorded as continuous scans in both fluorescence and transmission modes at ambient temperature and pressure in the range of -150 to 1000 eV around the edge in 180 s. The fluorescence data were used for the evaluation due to the better quality. For calibration, a copper foil was measured as a reference simultaneously with the samples.

The data treatment was performed using the Demeter software package.⁶⁰ To compensate for the oversampling of the continuous scan mode, the data points of the obtained spectra were reduced with the help of the “rebin”-function of Athena software (edge region: -50 to $+50\text{ eV}$; pre-edge grid: 5 eV ; XANES grid: 0.5 eV ; EXAFS grid: 0.05 \AA^{-1}). For data evaluation, a Victoreen-type polynomial was subtracted from the spectrum to remove the background using Athena software. The first inflection point was taken as edge energy E_0 . No phase shift corrections have been applied. The EXAFS analysis was performed using Artemis software. Prior to the fitting procedure, the amplitude reduction factor S_0^2 was determined for the Cu reference foil and used as a fixed parameter for all materials.

4.9. Catalytic Oxidation Reactions. Oxidation reactions were carried out in a 100 mL autoclave reactor equipped with a Teflon liner (Parr Instrument). About 25 mg of the catalyst was dispersed in 30 mL of acetonitrile. Cyclohexene (20 mmol) and 4.5 mmol of 1,2-dichlorobenzene as the internal standard for GC analysis were added. The autoclave was purged with oxygen three times and pressurized to 10 bar. Subsequently, the reaction mixture was heated to $80\text{ }^\circ\text{C}$. The reaction was initiated by switching on the stirrer at $75\text{ }^\circ\text{C}$. Equally, stirring was started at $5\text{ }^\circ\text{C}$ below the set temperature for oxidation reactions performed at different temperatures. Control experiments were carried out by varying the stirring speed using 400, 500, 600, and 700 rpm to investigate the influence of mass transfer (Figure S11). It can be observed that there is no further increase in conversion at 600 and 700 rpm, suggesting the absence of external mass transfer resistance with respect to the overall reaction rate. Therefore, a stirring speed of 600 rpm was chosen for the catalytic reactions.

Samples were taken through an online sampling system after 1, 2, 4, and 6 h. For GC analysis, two samples of 1.5 mL were taken after filtering off the catalyst with a syringe filter (200 nm). One sample was purely analyzed while the other was treated with 2 mmol triphenylphosphine (PPh_3) to decompose the formed 2-cyclohexene-1-hydroperoxide into the corresponding alcohol 2-cyclohexene-1-ol. The hydroperoxide amount was calculated by subtraction of the detected alcohol amounts. The deviation of the GC analysis is below 0.5%. The experiments are reproducible, leading to a typical deviation below 2%.

For homogeneously catalyzed cyclohexene oxidation, 1.1 mg of Cu(I) iodide (0.0059 mmol corresponding to 1.5% Cu on g- C_3N_4) was used under otherwise standard conditions.

To test the reusability of the catalyst, four reaction runs were carried out under standard conditions. After each run, the catalyst was separated by centrifugation, washed three times with 5 mL of acetonitrile and dried overnight at room temperature. The catalyst amount decreased from an initial 25 mg, to 23, 20, and 18 mg in the second, third, and fourth run, respectively.

For the investigation of cyclohexene oxidation in the presence of H_2O , 2 mL of H_2O was added to the initial standard solution, whereas all other reaction conditions remained unchanged.

To verify a radical mechanism, 20 mol % hydroquinone relative to the molar amount of cyclohexene was added to the standard solution, and all other reaction conditions were kept constant, too.

4.10. Synthesis of 2-Cyclohexene-1-hydroperoxide.

About 750 mg of 2,2'-azobis-2-dimethylpropionitrile as the radical initiator, 1 mL of 1,2-dichlorobenzene as the internal standard for GC analysis, and 30 mL of cyclohexene were filled in a 50 mL two-neck round bottom flask equipped with a reflux condenser. The solution was heated to 40 °C and bubbled with 20 mL min⁻¹ O₂ under stirring for 48 h. Afterward, the temperature was set to 30 °C for an additional 4 h. The obtained colorless, highly viscous solution was diluted with MeCN and analyzed by GC analysis. Its composition was determined to be 65.0% 2-cyclohexene-1-hydroperoxide, 10.5% 2-cyclohexene-1-one, 9.5% 7-oxabicyclo[4.1.0]-heptane-2-one, 4.9% cyclohexane-1,2-diol, 4.7%, 2-cyclohexene-1-ol, 4.4% cyclohexene oxide, and 1.4% cyclohexene.

4.11. Time-Resolved *In Situ* ATR-IR Spectroscopy. *In situ* ATR-IR spectroscopy was carried out with a ReactIR 15 from Mettler Toledo equipped with a diamond internal reflection element (IRE), a AgX 6 mm × 1.5 m fiber, and a liquid nitrogen cooled mercury–cadmium–telluride (MCT) detector. The spectral range of 3000–650 cm⁻¹ was recorded with a resolution of 4 cm⁻¹.

For detection of a characteristic signal of 2-cyclohexene-1-hydroperoxide, 30 mL of MeCN was filled in a beaker equipped with the IR probe. A background spectrum was recorded, which was used for background subtraction. Then, 1 mL of the synthesized 2-cyclohexene-1-hydroperoxide mixture was added three times and the corresponding spectra were recorded. Afterward, 1 mL solution of 1 g of triphenylphosphine (PPh₃) dissolved in 6 mL of MeCN was added six times, to selectively decompose the 2-cyclohexene-1-hydroperoxide stepwise into the corresponding alcohol 2-cyclohexene-1-ol.

For the *in situ* ATR-IR study, 125 mg of 1.5Cu-380 was suspended in 150 mL of acetonitrile. About 100 mmol of cyclohexene and 22.5 mmol of 1,2-dichlorobenzene as the internal standard for GC analysis were added. The reaction solution was filled in a Teflon liner of a 350 mL autoclave (Berghof) equipped with an ATR-IR probe (Mettler Toledo). The reactor was flushed three times with nitrogen and pressurized to 3 bar. It was heated in an inert atmosphere to 80 °C under stirring with 350 rpm. After the temperature was stabilized, the oxidation reaction was initiated by pressurizing the reactor with oxygen to 20 bar. The reaction progress was monitored by recording the spectra every 2 min. Meanwhile, samples were taken through an online sampling system after 0, 1, 2, 3, 4, and 6 h. For GC analysis, two samples of 1.5 mL were taken after the catalyst was filtered off using a syringe filter (200 nm) and analyzed by GC, as previously described, without and with PPh₃ treatment.

4.12. Gas Chromatography. Gas chromatography analysis was carried out in a 7820 A GC from Agilent Technologies. It was equipped with an Agilent DB-XLB column (30 m × 180 μm × 0.18 μm) and an FID detector. The injection volume was set to 0.5 μL with a split ratio of 75:1, a split flow of 30 mL min⁻¹, and an inlet temperature of 260 °C. The column was first kept at 80 °C for 5 min. Subsequently, the oven was heated to 170 °C with a rate of 15 °C min⁻¹. Afterward, it was heated with a ramp of 30 °C min⁻¹ up to 300 °C to avoid deposits of PPh₃ in the column. The end temperature was kept for 1 min.

■ ASSOCIATED CONTENT

Supporting Information

The Supporting Information is available free of charge at <https://pubs.acs.org/doi/10.1021/acscatal.1c01468>.

HAADF-TEM images of Cu single-atom catalysts; regional C 1s, N 1s, and Cu 2p XP spectra; surface composition and relative abundance of species derived from XP spectra; EXAFS and Fourier-transformed EXAFS spectra with fittings; catalytic data of cyclohexene oxidation over Cu single-atom catalysts as a function of time; effect of temperature on cyclohexene oxidation; XRD patterns of the recycled 1.5Cu-380 catalyst; synthesis of 2-cyclohexene-1-hydroperoxide; ATR-IR spectra of 2-cyclohexene-1-hydroperoxide; and time-resolved *in situ* ATR-IR spectra of cyclohexene oxidation (PDF)

■ AUTHOR INFORMATION

Corresponding Authors

Xiubing Huang – Laboratory of Industrial Chemistry, Ruhr University Bochum, 44780 Bochum, Germany; School of Materials Science and Engineering, University of Science and Technology Beijing, 100083 Beijing, China; orcid.org/0000-0002-3779-0486; Email: xiubinghuang@ustb.edu.cn

Baoxiang Peng – Laboratory of Industrial Chemistry, Ruhr University Bochum, 44780 Bochum, Germany; Max Planck Institute for Chemical Energy Conversion, 45470 Mülheim an der Ruhr, Germany; orcid.org/0000-0002-0972-3534; Email: baoxiang.peng@techem.rub.de

Authors

Julia Büker – Laboratory of Industrial Chemistry, Ruhr University Bochum, 44780 Bochum, Germany

Johannes Bitzer – Laboratory of Industrial Chemistry, Ruhr University Bochum, 44780 Bochum, Germany; Department of Chemistry, TU Kaiserslautern, 67663 Kaiserslautern, Germany

Wolfgang Kleist – Department of Chemistry, TU Kaiserslautern, 67663 Kaiserslautern, Germany; orcid.org/0000-0002-9364-9946

Martin Muhler – Laboratory of Industrial Chemistry, Ruhr University Bochum, 44780 Bochum, Germany; Max Planck Institute for Chemical Energy Conversion, 45470 Mülheim an der Ruhr, Germany; orcid.org/0000-0001-5343-6922

Complete contact information is available at: <https://pubs.acs.org/doi/10.1021/acscatal.1c01468>

Author Contributions

All authors have given approval to the final version of the manuscript.

Notes

The authors declare no competing financial interest.

■ ACKNOWLEDGMENTS

This research was funded by the Deutsche Forschungsgemeinschaft (DFG, German Research Foundation, Projektnummer 388390466—TRR 247). J. Büker acknowledges financial support as a fellow of the Evonik Stiftung. X.H. acknowledges financial support from Fundamental Research Funds for the Central Universities (QNXM20210016). The authors acknowledge DESY (Hamburg, Germany), a member of the Helmholtz Association HGF, for the provision of experimental facilities.

Parts of this research were carried out at PETRA III and the authors would like to thank Dr. Edmund Welter for assistance in using P65 (I-20191191). They also thank Dr. Heidelmann (Interdisciplinary Center for Analytics on the Nanoscale (ICAN), University of Duisburg-Essen) for transmission electron microscopy measurements. The authors acknowledge Mariia Merko and Philipp Schwiderowski (Chair of Industrial Chemistry, Ruhr-University Bochum) for ICP-MS and XPS measurements, respectively.

REFERENCES

- (1) Ameer, N.; Bachir, R.; Bedrane, S.; Choukchou-Braham, A. A Green Route to Produce Adipic Acid on TiO₂-Fe₂O₃ Nanocomposites. *J. Chin. Chem. Soc.* **2017**, *64*, 1096–1103.
- (2) Ghosh, S.; Acharyya, S. S.; Adak, S.; Konathala, L. N. S.; Sasaki, T.; Bal, R. Selective Oxidation of Cyclohexene to Adipic Acid over Silver Supported Tungsten Oxide Nanostructured Catalysts. *Green Chem.* **2014**, *16*, 2826.
- (3) de Vries, J. G.; Jackson, S. D. Homogeneous and Heterogeneous Catalysis in Industry. *Catal. Sci. Technol.* **2012**, *2*, 2009.
- (4) Damm, M.; Gutmann, B.; Kappe, C. O. Continuous-Flow Synthesis of Adipic Acid from Cyclohexene using Hydrogen Peroxide in High-Temperature Explosive Regimes. *ChemSusChem* **2013**, *6*, 978–982.
- (5) Rozhko, E.; Raabova, K.; Macchia, F.; Malmusi, A.; Righi, P.; Accorinti, P.; Alini, S.; Babini, P.; Cerrato, G.; Manzoli, M.; Cavani, F. Oxidation of 1,2-Cyclohexanediol to Adipic Acid with Oxygen: A Study Into Selectivity-Affecting Parameters. *ChemCatChem* **2013**, *5*, 1998–2008.
- (6) Rogers, O.; Pattison, S.; Engel, R. V.; Jenkins, R. L.; Whiston, K.; Taylor, S. H.; Hutchings, G. J. Adipic Acid Formation from Cyclohexanediol using Platinum and Vanadium Catalysts: Elucidating the Role of Homogeneous Vanadium Species. *Catal. Sci. Technol.* **2020**, *10*, 4210–4218.
- (7) da Silva, F. P.; Gonçalves, R. V.; Rossi, L. M. Magnetically Recoverable Copper Oxide Catalysts for Aerobic Allylic Oxidation of Cyclohexene. *J. Mol. Catal. A: Chem.* **2017**, *426*, 534–541.
- (8) Cai, Z.-Y.; Zhu, M.-Q.; Chen, J.; Shen, Y.-Y.; Zhao, J.; Tang, Y.; Chen, X.-Z. Solvent-Free Oxidation of Cyclohexene over Catalysts Au/OMS-2 and Au/La-OMS-2 with Molecular Oxygen. *Catal. Commun.* **2010**, *12*, 197–201.
- (9) Bükler, J.; Alkan, B.; Fu, Q.; Xia, W.; Schulwitz, J.; Waffel, D.; Falk, T.; Schulz, C.; Wiggers, H.; Muhler, M.; Peng, B. Selective Cyclohexene Oxidation with O₂, H₂O₂ and Tert-Butyl Hydroperoxide Over Spray-Flame Synthesized LaCo_{1-x}Fe_xO₃ nanoparticles. *Catal. Sci. Technol.* **2020**, *10*, 5196–5206.
- (10) Denekamp, I. M.; Antens, M.; Slot, T. K.; Rothenberg, G. Selective Catalytic Oxidation of Cyclohexene with Molecular Oxygen: Radical Versus Nonradical Pathways. *ChemCatChem* **2018**, *10*, 1035–1041.
- (11) Rogers, O.; Pattison, S.; Macginley, J.; Engel, R.; Whiston, K.; Taylor, S.; Hutchings, G. The Low Temperature Solvent-Free Aerobic Oxidation of Cyclohexene to Cyclohexane Diol over Highly Active Au/Graphite and Au/Graphene Catalysts. *Catalysts* **2018**, *8*, No. 311.
- (12) Cao, Y.; Yu, H.; Peng, F.; Wang, H. Selective Allylic Oxidation of Cyclohexene Catalyzed by Nitrogen-Doped Carbon Nanotubes. *ACS Catal.* **2014**, *4*, 1617–1625.
- (13) Ji, S.; Chen, Y.; Wang, X.; Zhang, Z.; Wang, D.; Li, Y. Chemical Synthesis of Single Atomic Site Catalysts. *Chem. Rev.* **2020**, *120*, 11900–11955.
- (14) Wu, Q.; Wei, W.; Lv, X.; Wang, Y.; Huang, B.; Dai, Y. Cu@g-C₃N₄: An Efficient Single-Atom Electrocatalyst for NO Electrochemical Reduction with Suppressed Hydrogen Evolution. *J. Phys. Chem. C* **2019**, *123*, 31043–31049.
- (15) Ong, W.-J.; Tan, L.-L.; Ng, Y. H.; Yong, S.-T.; Chai, S.-P. Graphitic Carbon Nitride (g-C₃N₄)-Based Photocatalysts for Artificial Photosynthesis and Environmental Remediation: Are We a Step Closer To Achieving Sustainability? *Chem. Rev.* **2016**, *116*, 7159–7329.
- (16) Gong, Y.; Li, M.; Li, H.; Wang, Y. Graphitic Carbon Nitride Polymers: Promising Catalysts or Catalyst Supports for Heterogeneous Oxidation and Hydrogenation. *Green Chem.* **2015**, *17*, 715–736.
- (17) Nilforoushan, S.; Ghiaci, M.; Hosseini, S. M.; Laurent, S.; Muller, R. N. Selective Liquid Phase Oxidation of Ethyl Benzene to Acetophenone by Palladium Nanoparticles Immobilized on a g-C₃N₄-rGO Composite as a Recyclable Catalyst. *New J. Chem.* **2019**, *43*, 6921–6931.
- (18) Muniandy, L.; Adam, F.; Mohamed, A. R.; Iqbal, A.; Rahman, N. R. A. Cu²⁺ Coordinated Graphitic Carbon Nitride (Cu-g-C₃N₄) Nanosheets from Melamine for the Liquid Phase Hydroxylation of Benzene and VOCs. *Appl. Surf. Sci.* **2017**, *398*, 43–55.
- (19) Wang, Y.; Wang, X.; Antonietti, M. Polymeric Graphitic Carbon Nitride as a Heterogeneous Organocatalyst: From Photochemistry to Multipurpose Catalysis to Sustainable Chemistry. *Angew. Chem., Int. Ed.* **2012**, *51*, 68–89.
- (20) Payra, S.; Saha, A.; Banerjee, S. On Water Cu@g-C₃N₄ Catalyzed Synthesis of NH-1,2,3-Triazoles via [2+3] Cycloadditions of Nitroolefins/Alkynes and Sodium Azide. *ChemCatChem* **2018**, *10*, 5468–5474.
- (21) Yang, J.; Zhang, H.; Chen, B.; Tang, H.; Li, C.; Zhang, Z. Fabrication of the g-C₃N₄/Cu Nanocomposite and Its Potential for Lubrication Applications. *RSC Adv.* **2015**, *5*, 64254–64260.
- (22) Inagaki, M.; Tsumura, T.; Kinumoto, T.; Toyoda, M. Graphitic Carbon Nitrides (g-C₃N₄) with Comparative Discussion to Carbon Materials. *Carbon* **2019**, *141*, 580–607.
- (23) Li, F.; Han, G.-F.; Noh, H.-J.; Kim, S.-J.; Lu, Y.; Jeong, H. Y.; Fu, Z.; Baek, J.-B. Boosting Oxygen Reduction Catalysis with Abundant Copper Single Atom Active Sites. *Energy Environ. Sci.* **2018**, *11*, 2263–2269.
- (24) Shi, G.; Yang, L.; Liu, Z.; Chen, X.; Zhou, J.; Yu, Y. Photocatalytic Reduction of CO₂ to CO over Copper Decorated g-C₃N₄ Nanosheets with Enhanced Yield and Selectivity. *Appl. Surf. Sci.* **2018**, *427*, 1165–1173.
- (25) Dai, Y.; Gu, Y.; Bu, Y. Modulation of the Photocatalytic Performance of g-C₃N₄ by Two-Sites Co-Doping Using Variable Valence Metal. *Appl. Surf. Sci.* **2020**, *500*, No. 144036.
- (26) Khan, M. A.; Mutahir, S.; Wang, F.; Zhen, H.; Lei, W.; Xia, M.; Ouyang, Y.; Muhmood, T. Synthesis of Environmentally Encouraged, Highly Robust Pollutants Reduction 3-D System Consisting of Ag/g-C₃N₄ and Cu-Complex to Degrade Refractory Pollutants. *J. Photochem. Photobiol., A* **2018**, *364*, 826–836.
- (27) Lan, H.; Tang, Y.; Zhang, X.; You, S.; Tang, Q.; An, X.; Liu, H.; Qu, J. Decomplexation of Cu(II)-EDTA over Oxygen-Doped g-C₃N₄: An Available Resource Towards Environmental Sustainability. *Chem. Eng. J.* **2018**, *345*, 138–146.
- (28) Zhang, P.; Song, T.; Wang, T.; Zeng, H. Effectively Extending Visible Light Absorption with a Broad Spectrum Sensitizer for Improving the H₂ Evolution of In-Situ Cu/g-C₃N₄ Nanocomponents. *Int. J. Hydrogen Energy* **2017**, *42*, 14511–14521.
- (29) Zhao, Z.; Sun, Y.; Dong, F. Graphitic Carbon Nitride Based Nanocomposites: A Review. *Nanoscale* **2015**, *7*, 15–37.
- (30) Zheng, Y.; Lin, L.; Wang, B.; Wang, X. Graphitic Carbon Nitride Polymers toward Sustainable Photoredox Catalysis. *Angew. Chem., Int. Ed.* **2015**, *54*, 12868–12884.
- (31) Zhang, T.; Zhang, D.; Han, X.; Dong, T.; Guo, X.; Song, C.; Si, R.; Liu, W.; Liu, Y.; Zhao, Z. Preassembly Strategy To Fabricate Porous Hollow Carbonitride Spheres Inlaid with Single Cu-N₃ Sites for Selective Oxidation of Benzene to Phenol. *J. Am. Chem. Soc.* **2018**, *140*, 16936–16940.
- (32) Li, Z.; Kong, C.; Lu, G. Visible Photocatalytic Water Splitting and Photocatalytic Two-Electron Oxygen Formation over Cu- and Fe-Doped g-C₃N₄. *J. Phys. Chem. C* **2016**, *120*, 56–63.
- (33) Le, S.; Jiang, T.; Zhao, Q.; Liu, X.; Li, Y.; Fang, B.; Gong, M. Cu-Doped Mesoporous Graphitic Carbon Nitride for Enhanced Visible-Light Driven Photocatalysis. *RSC Adv.* **2016**, *6*, 38811–38819.
- (34) Zou, X.; Silva, R.; Goswami, A.; Asefa, T. Cu-Doped Carbon Nitride: Bio-Inspired Synthesis of H₂-Evolving Electrocatalysts Using

Graphitic Carbon Nitride (g-C₃N₄) as a Host Material. *Appl. Surf. Sci.* **2015**, *357*, 221–228.

(35) Sarkar, S.; Sumukh, S. S.; Roy, K.; Kamboj, N.; Purkait, T.; Das, M.; Dey, R. S. Facile One Step Synthesis of Cu-g-C₃N₄ Electrocatalyst Realized Oxygen Reduction Reaction with Excellent Methanol Crossover Impact and Durability. *J. Colloid Interface Sci.* **2020**, *558*, 182–189.

(36) Wang, L.; Zhu, Y.; Yang, D.; Zhao, L.; Ding, H.; Wang, Z. The Mixed Marriage of Copper and Carbon Ring-g-C₃N₄ Nanosheet: A Visible-Light-Driven Heterogeneous Fenton-Like Catalyst. *Appl. Surf. Sci.* **2019**, *488*, 728–738.

(37) Chen, X.; Zhang, J.; Fu, X.; Antonietti, M.; Wang, X. Fe-g-C₃N₄-Catalyzed Oxidation of Benzene to Phenol Using Hydrogen Peroxide and Visible Light. *J. Am. Chem. Soc.* **2009**, *131*, 11658–11659.

(38) Marcinkowski, M. D.; Darby, M. T.; Liu, J.; Wimble, J. M.; Lucci, F. R.; Lee, S.; Michaelides, A.; Flytzani-Stephanopoulos, M.; Stamatakis, M.; Sykes, E. C. H. Pt/Cu Single-Atom Alloys as Coke-Resistant Catalysts for Efficient C-H Activation. *Nat. Chem.* **2018**, *10*, 325–332.

(39) Yan, Q.; Zhao, C.; Zhang, L.; Hou, Y.; Wang, S.; Dong, P.; Lin, F.; Wang, Y. Facile Two-Step Synthesis of Porous Carbon Nitride with Enhanced Photocatalytic Activity Using a Soft Template. *ACS Sustainable Chem. Eng.* **2019**, *7*, 3866–3874.

(40) Ding, Z.; Chen, X.; Antonietti, M.; Wang, X. Synthesis of Transition Metal-Modified Carbon Nitride Polymers for Selective Hydrocarbon Oxidation. *ChemSusChem* **2011**, *4*, 274–281.

(41) AlOthman, Z. A Review: Fundamental Aspects of Silicate Mesoporous Materials. *Materials* **2012**, *5*, 2874–2902.

(42) Yan, H. Soft-Templating Synthesis of Mesoporous Graphitic Carbon Nitride with Enhanced Photocatalytic H₂ Evolution Under Visible Light. *Chem. Commun.* **2012**, *48*, 3430–3432.

(43) Jin, Z.; Zhang, L. Performance of Ni-Cu Bimetallic Co-Catalyst g-C₃N₄ Nanosheets for Improving Hydrogen Evolution. *J. Mater. Sci. Technol.* **2020**, *49*, 144–156.

(44) Biesinger, M. C. Advanced Analysis of Copper X-Ray Photoelectron Spectra. *Surf. Interface Anal.* **2017**, *49*, 1325–1334.

(45) Hu, S.; Qu, X.; Bai, J.; Li, P.; Li, Q.; Wang, F.; Song, L. Effect of Cu(I)–N Active Sites on the N₂ Photofixation Ability over Flowerlike Copper-Doped g-C₃N₄ Prepared via a Novel Molten Salt-Assisted Microwave Process: The Experimental and Density Functional Theory Simulation Analysis. *ACS Sustainable Chem. Eng.* **2017**, *5*, 6863–6872.

(46) Ene, A. B.; Bauer, M.; Archipov, T.; Roduner, E. Adsorption of Oxygen on Copper in Cu/HZSMS Zeolites. *Phys. Chem. Chem. Phys.* **2010**, *12*, 6520–6531.

(47) Drake, I. J.; Furdala, K. L.; Baxamusa, S.; Bell, A. T.; Tilley, T. D. Effects of Precursor Composition on the Local Structure of Cu Dispersed on Mesoporous Silica: A Detailed X-ray Absorption Spectroscopy Study. *J. Phys. Chem. B* **2004**, *108*, 18421–18434.

(48) Lambell, G.; Moen, A.; Nicholson, D. G. Structure of the Diamminecopper(I) Ion in Solution. An X-Ray Absorption Spectroscopic Study. *Faraday Trans.* **1994**, *90*, No. 2211.

(49) Xiao, X.; Gao, Y.; Zhang, L.; Zhang, J.; Zhang, Q.; Li, Q.; Bao, H.; Zhou, J.; Miao, S.; Chen, N.; Wang, J.; Jiang, B.; Tian, C.; Fu, H. A Promoted Charge Separation/Transfer System from Cu Single Atoms and C₃N₄ Layers for Efficient Photocatalysis. *Adv. Mater.* **2020**, *32*, No. e2003082.

(50) Shreve, O. D.; Heether, Knight, H. B.; Swern, D. Infrared Absorption Spectra of Some Hydroperoxides, Peroxides, and Related Compounds. *Anal. Chem.* **1951**, *23*, 282–285.

(51) Nowotny, M.; Pedersen, L. N.; Hanefeld, U.; Maschmeyer, T. Increasing the Ketone Selectivity of the Cobalt-Catalyzed Radical Chain Oxidation of Cyclohexane. *Chem. - Eur. J.* **2002**, *8*, 3724–3731.

(52) Liang, H.-C.; Kim, E.; Incarvito, C. D.; Rheingold, A. L.; Karlin, K. D. A Bis-Acetonitrile Two-Coordinate Copper (I) Complex: Synthesis and Characterization of Highly Soluble B(C₆F₅)₄-Salts of [Cu(MeCN)₂]⁺ and [Cu(MeCN)₄]⁺. *Inorg. Chem.* **2002**, *41*, 2209–2212.

(53) Liu, W.; Zhang, L.; Liu, X.; Liu, X.; Yang, X.; Miao, S.; Wang, W.; Wang, A.; Zhang, T. Discriminating Catalytically Active Fe_Nx Species

of Atomically Dispersed Fe–N–C Catalyst for Selective Oxidation of the C–H Bond. *J. Am. Chem. Soc.* **2017**, *139*, 10790–10798.

(54) Wang, W.; Sharapa, D. I.; Chandresh, A.; Nefedov, A.; Heißler, S.; Heinke, L.; Studt, F.; Wang, Y.; Wöll, C. Interplay of Electronic and Steric Effects to Yield Low-Temperature CO Oxidation at Metal Single Sites in Defect-Engineered HKUST-1. *Angew. Chem., Int. Ed.* **2020**, *59*, 10514–10518.

(55) Wu, H.; Li, H.; Zhao, X.; Liu, Q.; Wang, J.; Xiao, J.; Xie, S.; Si, R.; Yang, F.; Miao, S.; et al. Highly Doped and Exposed Cu(I)–N Active Sites Within Graphene Towards Efficient Oxygen Reduction for Zinc–Air Batteries. *Energy Environ. Sci.* **2016**, *9*, 3736–3745.

(56) Kochi, J. K. The Mechanism of the Copper Salt Catalyzed Reactions of Peroxides. *Tetrahedron* **1962**, *18*, 483–497.

(57) Klinman, J. P. Mechanisms Whereby Mononuclear Copper Proteins Functionalize Organic Substrates. *Chem. Rev.* **1996**, *96*, 2541–2562.

(58) Fontecave, M.; Pierre, J.-L. Oxidations by Copper Metalloenzymes and Some Biomimetic Approaches. *Coord. Chem. Rev.* **1998**, *170*, 125–140.

(59) Welter, E.; Chernikov, R.; Herrmann, M.; Nemausat, R. A Beamline for Bulk Sample X-Ray Absorption Spectroscopy at the High Brilliance Storage Ring PETRA III. *AIP Conf. Proc.* **2019**, No. 040002.

(60) Ravel, B.; Newville, M. ATHENA, ARTEMIS, HEPHAESTUS: Data Analysis for X-Ray Absorption Spectroscopy Using IFEFFIT. *J. Synchrotron Radiat.* **2005**, *12*, 537–541.